Chalcogenide Letters Vol. 22, No. 4, April 2025, p. 313 - 330

Molybdenum disulfide carbon composite material using hydrothermal method as electrode material for supercapacitors

X. L. Guo [a], Y. F. Zhang [a,*], S. Y. Li[b], Q. Li [b], Q. Hao [c], X. Y. Ran [c], Y. M. Zhao [d]
[a] *School of Mechanical Engineering, Qilu University of Technology (Shandong Academy of Sciences), Jinan, Shandong, 250353, PR China*
[b] *School of Material Science and Engineering, Qilu University of Technology (Shandong Academy of Sciences), Jinan, Shandong, 250353, PR China*
[c] *Weihai Yinxing Prestressed Wire Products Co., Ltd, Weihai, Shandong, 264200, China*
[d] *Shandong Hi-Speed New Materials Group Co., Ltd, 250000, China*

MoS_2 has excellent properties but low conductivity, limiting its use in supercapacitors. Carbon's high conductivity and stability enhance MoS_2's electrochemical performance and cycling stability. This study prepared MoS_2/C composites via a one-step hydrothermal method, exploring the effects of solvents and carbon content. Deionized water as a solvent resulted in composites with large specific surface areas and good electrochemical properties. Increasing carbon content improved electrochemical performance, peaking at a glucose content of 0.28 mmol, achieving a specific capacitance of 202.6 F/g. However, excessive carbon content led to decreased performance.

(Received January 13, 2025; Accepted April 7, 2025)

Keywords: MoS_2/C composites, Supercapacitors, Electrode materials

1. Introduction

In the context of technological innovation and societal development, the demand for traditional energy sources such as coal, minerals, oil and natural gas remains exceptionally high. Because they are not renewable energy, their content on the earth cannot be restored in a short time, so we have an increasingly urgent need for the development of clean, renewable and sustainable energy [1]. Additionally, as society increasingly relies on energy storage technology, there is an escalating need to create compact, efficient, and versatile energy storage systems to address existing limitations. Therefore, the storage technology of renewable energy sources has become a core problem to be solved urgently, and in order to use these energy sources efficiently, we need to integrate them into advanced energy storage systems so as to achieve their effective preservation and flexible use [2]. The most prevalent energy storage technologies in use today are rechargeable batteries and supercapacitors. Each has its own set of advantages and disadvantages: rechargeable

* Corresponding authors: zhangyanfei@qlu.edu.cn
https://doi.org/10.15251/CL.2025.224.313

batteries, with their high energy content, can retain a greater amount of energy within an equivalent space, while supercapacitors provide rapid charging speeds, high power output, long cycle life, and flexible working modes [3-6]. The research in this paper will aim to strengthen the energy content of supercapacitors for different applications, hopefully by optimizing the electrode materials with the purpose of strengthening their energy storage capacity.

Supercapacitors, a novel energy storage device, are located between secondary batteries and traditional capacitors, and their core components mainly include electrode materials, fluid collectors, electrolytes, and diaphragms [7-10]. Compared to traditional capacitors, supercapacitors demonstrate significant performance advantages. They exhibit excellent specific capacitance and specific energy, a wider operating temperature range, and longer cycle life. Notably, in terms of energy density, supercapacitors far surpass traditional capacitors, with values reaching 10 to 100 times higher. Furthermore, compared to lithium batteries, supercapacitors also possess unique characteristics. Their specific power is particularly outstanding as they can discharge a large current in a very short time and feature fast charging speed, high charging efficiency, and long cycle life. Importantly, supercapacitors have minimal environmental impact and are less polluting [11-14]. Supercapacitors also have certain limitations, such as low energy density. In comparison to traditional batteries, supercapacitors exhibit a lower energy density, resulting in less energy storage per unit volume or weight. This restricts the use of supercapacitors in applications requiring prolonged and high-energy supply. In order to overcome these drawbacks, the selection and development of electrode materials are particularly important. Therefore, the development and expansion of electrode materials with superior performance has become one of the key directions to enhance the electrochemical performance of supercapacitors [15-18]. Currently, the electrode materials applied to supercapacitors mainly comprise carbon materials, transition metal oxides/sulfides, and conductive polymers.

In recent years, transition metal sulfides (TMDs) have had a profound effect on the development of li-ion batteries and supercapacitors by virtue of their unique construction and high capacity performance, with MoS_2 being the primary focus among transition metal sulfides. MoS_2 is a graphene-like layered compound, composed of single or multiple layers [19-23].There are three distinct phase states of MoS_2, as depicted in Fig. 1 namely the 1T phase with an octahedral structure, and the 2H and 3R phases with triprism structures. The disparity among these phase states primarily arises from variations in atomic arrangement and layer stacking modes, collectively determining the diverse phase characteristics of MoS_2 [24-27]. 1T-MoS_2 has an octahedrally coordinated crystal structure in which sulfur and molybdenum atoms are arranged in a special way so that this phase of molybdenum disulfide exhibits metallic properties and belongs to a substable structure. T may represent a simplification of “Tetrahedral” or “Trigonal”, which is used to characterize the geometry of the atomic arrangement in this phase. The 2H-MoS_2 crystalline phase comprises two Mo-S layers and represents a structurally stable configuration. In the layered structure, a configuration resembling a "sandwich" is created, comprising a double layer of sulfur atoms encased within a hexagonally arranged level of metal atoms. Within these layers, the Mo-S bonds are predominantly covalent, whereas the interlayer interactions are sustained by weaker van der Waals forces. H may stand for some abbreviation or simplification of “Hexagonal” or “Highly Symmetric”. 3R-MoS_2 has one additional Mo-S unit compared to 2H-MoS_2, meaning it comprises three Mo-S units and is a metastable structure. R may stand for some variation or simplification of “Rhombohedral” or “Rotated”. Furthermore, these identifiers

(T, H, R) are not absolute or uniform nomenclature. Different symbols or terms may be used in different literature or research areas to describe different phases of molybdenum disulfide.

The MoS_2 exhibits high theoretical specific capacity and cost-effectiveness, making it an ideal active material [28-34]. Nevertheless, pure MoS_2 exhibits inherent drawbacks such as structural instability and poor electrical conductivity, leading to a significant reduction in discharge capacity and shortened material service life [35]. The main improvement measures are: morphology control, interface modification, structural design and doping. Mabkhoot Alsaiariet et al. [36] synthesized the NiCoS@MoS2@rGO composite for use in supercapacitor electrodes and electrochemical glucose sensors. This design concept can also be extended to inorganic materials, enabling the development of multifunctional, multi-component hybrid materials. Such materials hold significant potential for a wide range of applications, including energy storage and biomedical fields. The composite electrode material exhibited a high specific capacity of 301 C/g, along with energy and power densities of 65.44 Wh/kg and 1267.18 W/kg, respectively, at a current density of 1 A/g. After 5000 charge/discharge cycles, the electrode achieved a Coulombic efficiency of 92.79% and a capacity retention of 83.42%. Rimjhim Yadav et al.[37] synthesized two distinct forms of polypyrrole and MoS_2 nanostructured binary nanocomposites using in-situ polymerization technology. The PPyNTs/MoS_2 nanocomposites consist of PPyNTs tightly wrapped around MoS_2, exhibiting a specific capacitance of 481 F/g at 0.5 A/g. After 2000 charge/discharge cycles, the specific capacitance of the PPyNTs/MoS_2 composite only decreased by 5.6%. In order to fully leverage the advantages of MoS_2 and mitigate the limitations of a single compound, a MoS_2/C composite material was prepared via a one-step hydrothermal approach. The selection of glucose as the carbon source, due to its simplicity, ready availability, and cost-effectiveness, effectively controls costs.

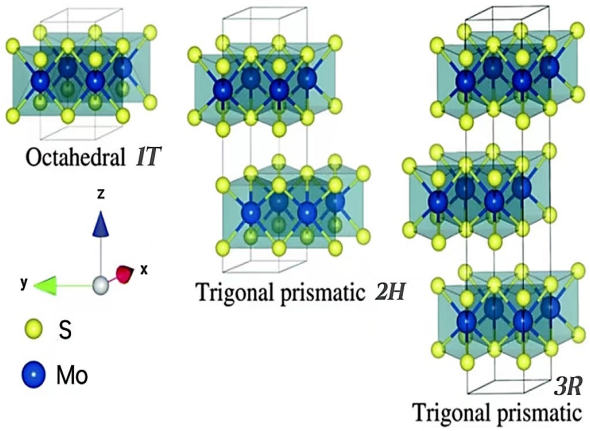

Fig. 1. Three phase of MoS_2.

2. Experimental section

2.1. Chemicals and reagents

Ammonium molybdate tetrahydrate ($(NH_4)_2MoO_4 \cdot 4H_2O$) was purchased from Shanghai Aladdin Biochemical Technology Co. Thiourea (CH_4N_2S), urea (CH_4N_2O), glucose ($C_6H_{12}O_6$) were purchased from Tianjin Damao Chemical Reagent Factory. Acetylene black,

polytetrafluoroethylene (PTFE) were purchased from Guangdong Candlelight New Energy Technology Co. Anhydrous ethanol (C_2H_6O) was purchased from Tianjin Fuyu Fine Chemical Co. Sodium hydroxide (NaOH) was purchased from Guangzhou Hewei Pharmaceutical Co. Dilute hydrochloric acid solution (HCl) was purchased from Xi'an Tianmao Chemical Co. All chemicals were used as starting materials without further purification.

2.2. Preparation of MoS_2/C composite materials

In this paper, the Single-step hydrothermal process was employed to synthesize MoS_2/C composite material, which is a commonly used approach for fabricating MoS_2 composite materials. The precursor was dissolved in an appropriate solvent using ultrasonic or stirring methods to ensure thorough mixing, and the homogeneous mixture was then placed in a high-pressure reactor for the reduction process. The reaction must be conducted under constant temperature conditions, typically at 180 ℃ or higher, and maintained for a minimum of 15 hours. First, use an electronic balance to weigh 0.98 g of ammonium molybdate and 1.14 g of thiourea. Dissolve the materials in 40 mL of deionized water under continuous stirring until a homogeneous solution is obtained. Then, add 0.24 g of carbamide and continue stirring for 30 minutes. Separately, dissolve 0.07 mmol, 0.14 mmol, 0.28 mmol, 0.56 mmol, 1.12 mmol, or 2.24 mmol of glucose in the prepared solution, stirring again until fully dissolved. The solution is transferred to a 100 mL high-temperature reactor and heated in an oven at 180 ℃ for 24 hours. After it had naturally cooled to normal temperature, it underwent multiple centrifugation cycles and was thoroughly washed using anhydrous ethanol and deionized water then dried for 8 hours at 180 ℃, and finally the samples were obtained. The samples were labeled. In another set of parallel experiments, we did not add glucose, but instead used anhydrous ethanol and deionized water as solvents separately, while keeping the amounts of ammonium molybdate, thiourea, and urea unchanged. The entire experimental procedure is schematically illustrated in Scheme 1.

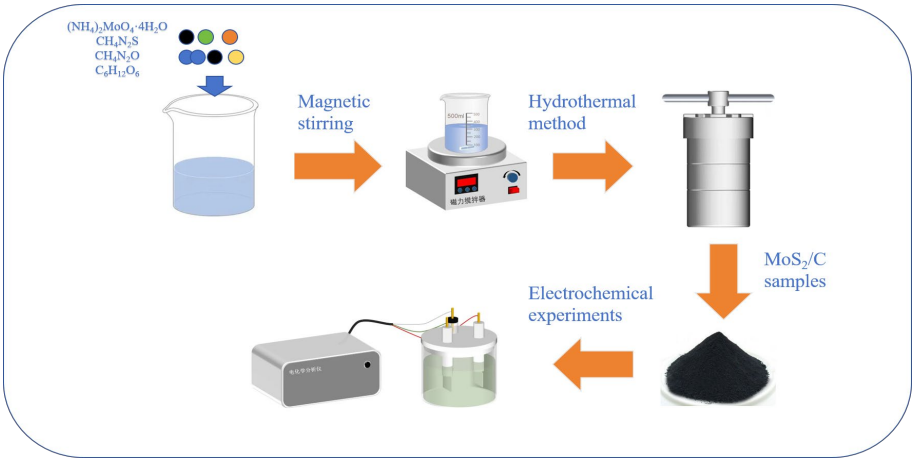

Scheme 1. Schematic diagram of the experimental procedure for MoS_2/C composites.

2.3. Fabrication of electrodes

Porous nickel foam was used as the current collector for the supercapacitor, and the pre-treated nickel foam was cut into small rectangles of 1.5×1 cm^2 , dried and weighed and denoted as m_1. The electrode material, acetylene black, and PTFE were mixed in an 8:1:1 mass

ratio, and then stirred in anhydrous ethanol to ensure that the three components were homogeneously mixed. The mixture was uniformly coated onto the nickel foam substrate after blending. Immediately thereafter, the nickel foam coated with the mixed material was transferred to a drying oven. After drying at 90 ℃ for 12 h, it was removed and weighed and recorded as m_2. The coating area is 1×1 cm^2, with the active mass varying between 0.5 mg and 2.5 mg. The weight of the electrode material coated on the nickel foam is $m=0.8\ (m_2-m_1)$.

2.4. Characterization and testing

Firstly, X-ray diffraction (XRD) analysis was performed, and the sample's XRD pattern was obtained using an X-ray diffractometer, the XRD instrument model is SHIMADZU XRD-6100 from Japan. Before testing, a certain mass of sample powder was placed in the sample tank and flattened with a slide. The test was then conducted at a scanning speed of 6°/min, covering an angle range of 10° to 80°. Next, X-ray photoelectron spectroscopy (XPS) characterization analysis is carried out to analyze the empirical chemical formulas, as well as the chemical composition and electronic properties of various elements in the material. XPS instrument model ESCALABXi+, firstly, a double-sided adhesive tape of about 2 cm×2 cm is pasted on the aluminum foil, and the powder to be tested is uniformly coated on the double-sided adhesive tape surface, and then placed on the tableting machine after folding the aluminum foil to be tabletted, and the pressure is applied to After the foil is folded and placed on the tablet press, the pressure is applied to about 6MP, after the tablet press is completed, the sample making process is finished. Scanning electron microscopy (SEM) characterization is then performed. The first step is to prepare a metal specimen, followed by the emission of high-energy electrons from the SEM instrument (Zeiss G500), which are then struck on the metal specimen and the secondary electrons formed from the high-energy electrons generated by the sputtering are collected, and the final imaging of the secondary electrons is then used to obtain a graphical representation of the surface appearance of the material. Finally, electrochemical characterization analysis was carried out. Electrochemical analysis has three parts, which are: CV (Cyclic Voltammetry), GCD (Galvanostatic charging/discharging) and EIS (Electrochemical Impedance Spectroscopy). This method involves measuring the changes in potential, current, and electric quantity of a chemical battery by leveraging the electrochemical properties of a substance, and subsequently analyzing the obtained results. The CV curve serves as a tool to examine the influence of the intercalation current produced by MoS_2 and the reaction mechanisms across various voltages. Additionally, the specific capacitance of the electrode material can be derived from the CV curve.

As indicated in the formula:

$$C = \frac{\int idV}{2mv\Delta V} \tag{1-1}$$

In the formula, C is the specific capacitance of the electrode material ($F \cdot g^{-1}$); $\int idV$ is the area integral of the measured CV curve; m is the mass of the active material (mg); V is the scanning rate (mV/s); ΔV is the voltage window (V). The specific capacitance of the electrode material can be calculated from the GCD curve. As indicated in the formula:

$$C = \frac{I \cdot \Delta t}{m \cdot \Delta V} \tag{1-2}$$

In the formula, C is the specific capacitance of the electrode material ($F \cdot g^{-1}$); I is the discharge current (A); m is the mass of the active material (mg); ΔV is the voltage window (V).

The EIS curve is composed of two distinct segments: a semicircle observed at higher frequencies and a linear slope appearing at lower frequencies. The radius of this half circle, in the higher frequency range, represents the interfacial resistance at the electrode-electrolyte junction, along with the magnitude of charge transfer, both of which exhibit a direct proportionality. On the other hand, the slope of the linear portion in the lower frequency range reflects the resistance caused by ion diffusion through the electrode material, displaying an inverse proportionality.

3. Results and discussion

3.1. Characterization and analysis of MoS_2 under different solvent conditions

The X-ray diffraction (XRD) spectrum of Fig. 2 presents the MoS_2 material synthesized using a single-step hydrothermal synthesis under the conditions of two different solvent systems, and its structure was characterized in detail by X-ray diffraction techniques. Fig. 2 (a) clearly displays the diffraction peaks of the samples MoS_2-deionized water and MoS_2-Anhydrous ethanol at the angle range of 10° to 80° between the incident X-ray beam and the diffraction detector, and this wide range of angles helps to comprehensively capture and analyze the crystalline structure characteristics of MoS_2 in different solvent environments. Fig.2 (b) is a fine presentation of the localized XRD pattern from 30° to 60°, which focuses on the diffraction peaks within this specific interval to allow for a more in-depth observation and analysis of the crystal structure differences or similarities of MoS_2 in the two solvents. Through such graphical representations, researchers can delve more deeply into the potential effects of interactions between MoS_2 and various solvents on its crystal structure. It is evident from the images that the samples prepared using the two solvents all exhibit relatively sharp diffraction peaks at 2θ=14.1° for the (002) plane, 2θ=32.6° for the (100) plane, and 2θ=39.6° for the (103) plane. But these diffraction peaks of MoS_2-deionized water samples are significantly more prominent in terms of their apparent intensity, indicating that they are highly crystalline. Meanwhile, no obvious impurity peaks could be observed in the image, which further confirms the good purity of the sample. The magnified XRD patterns in Fig. 2 (b), reveal distinct diffraction peaks at 33.5°, 33.9°, 44.2°, and 56.0°, which are assigned to the (101), (102), (104), and (106) crystallographic planes, respectively. At these specific diffraction angles, the diffraction peaks of the MoS_2-deionized water sample are more prominent. In contrast, the MoS_2-Anhydrous ethanol sample does not exhibit corresponding diffraction peaks. This phenomenon suggests that the samples prepared using deionized water have better crystal development and a richer crystallographic phase content. The degree of perfection of the crystal development is directly related to the ordered arrangement of the atoms or molecules within it, and this high degree of ordering is capable of generating more intense diffraction signals, thus further confirming the superiority of the MoS_2 samples made with deionized water in terms of crystal structure and purity [38-41].

Overall, the XRD patterns and PDF cards of both samples exhibited good consistency, confirming the precision and dependability of the experimental data while also indirectly demonstrating the reliability of the testing method. In particular, when deionized water was used as the solvent, the prepared samples exhibited higher purity and their crystal structures were more complete. This finding highlights the importance of solvent selection in influencing the quality and crystal structure of the samples, and also provides a useful reference for further optimization of the preparation process.

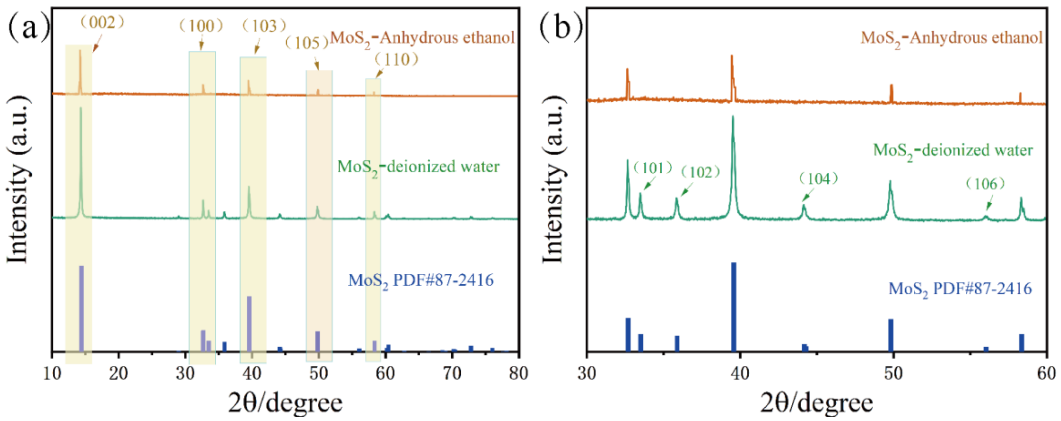

Fig. 2. XRD under different solvent conditions.

The MoS_2 materials, synthesized using deionized water and ethanol as solvents, were examined through SEM and their analysis is presented in Fig. 3 (a) and (b). It is evident from the figure that the morphology of both products, regardless of whether deionized water or ethanol was used as the solvent, is spherical, and the degree of dispersion is relatively homogeneous. However, when deionized water is used as the solvent, the spheres exhibit large lamellar structures composed of numerous flakes resembling a flower ball. In contrast, when ethanol is used as the solvent, the surface is smooth, with an obvious bright spot inside. It is hypothesized that this bright spot may indicate a nucleation phenomenon. This could be due to the fact that deionized water has a higher boiling point than anhydrous ethanol. When ethanol is used as a solvent, the reaction may result in volatilization due to temperature increase, creating an environment of increased pressure, which promotes nucleation. After the formation of numerous nuclei, some may dissolve, while others continue to grow. Finally, the surface pits are filled with Mo^{4+} and S^{2-} ions from the solution by diffusion, resulting in a smooth surface. This causes the spheres to be closely packed, enhancing viscosity while decreasing the surface area and electrochemical performance of the material.

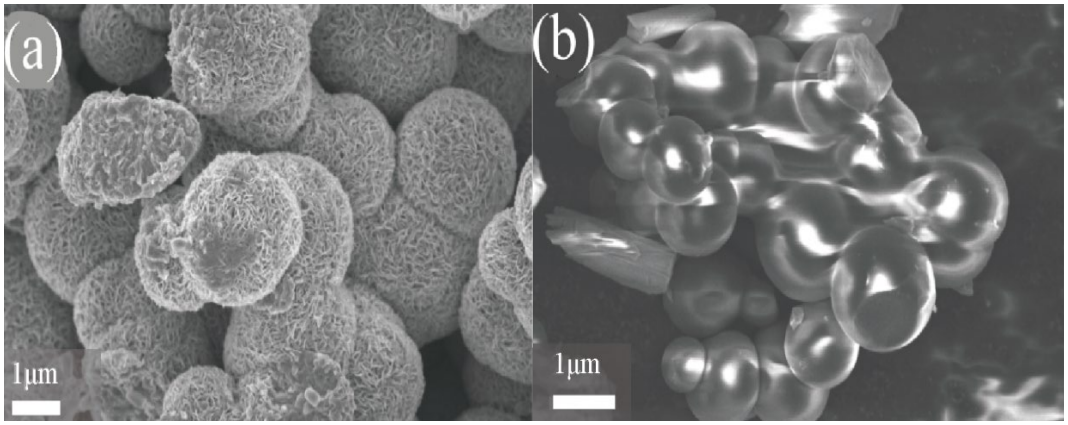

Fig. 3. (a) SEM with deionized water as solvent; (b) SEM with ethanol as solvent.

As demonstrated by Fig. 4 (a), which is a cyclic voltammetry test of MoS_2 electrode material under the conditions of different solvents, the CV curves obtained with deionized water as the solvent appear smoother and enclose a larger area. This indicates greater specific capacitance and better electrochemical performance of the electrode materials when deionized water is used as a solvent, and these findings align with the characterization results from XRD and SEM studies [42-44]. Fig. 4 (b) presents the constant current charge/discharge test conducted under varying solvent conditions at a current density of 1 A/g. The figure indicates that the curves exhibit a certain symmetry regardless of the solvent used. Calculations show that the capacitance reaches 96.6 F/g with anhydrous ethanol as the solvent, while deionized water yields 137.8 F/g. The impedance test in Fig. 4 (c) illustrates the impact of different solvent conditions. At low frequencies, the line's slope represents ion transfer and diffusion resistance in the electrode material. The diameter of the high-frequency region and semicircle correspond to ion transfer impedance at the electrode-electrolyte interface [45-47]. It is evident from the curves that deionized water as a solvent result in a smaller radius compared to anhydrous ethanol, indicating lower charge transfer impedance, faster electrode interface reaction speed, and better charge-discharge performance. We conducted constant-current charge/discharge tests on two sets of samples across varying current densities (0.5A/g, 1A/g, 2A/g, and 4A/g) to determine their specific capacitance under different loading conditions. Additionally, we calculated the decay rate using the formula $\eta=(C_1-C_2)/C_1$ where η represents the decay rate of specific capacitance, C_1 is the specific capacitance at 0.5A/g, and C_2 corresponds to the specific capacitance at varying current densities. The resulting histogram depicted in Fig. 4 (d) reveals a trend: as the current density progressively rises, the attenuation rate also exhibits a continuous increase. This suggests that traditional MoS_2 material fails to sustain an optimal specific capacitance under high current densities.

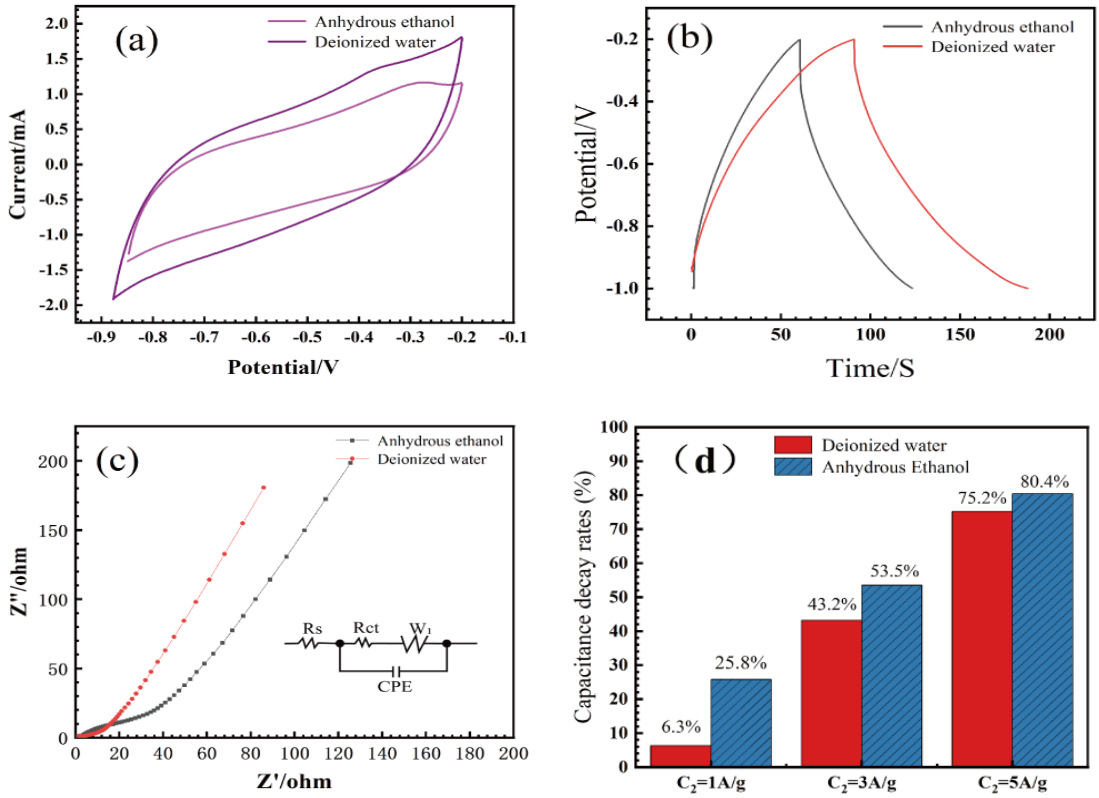

Fig. 4. (a) CV curves under different solvent conditions; (b) GCD curve under different solvent conditions; (c) EIS curve under different solvent conditions; (d) Bar charts of attenuation rates under different solvent conditions.

3.2. Characterization and analysis of MoS_2/C composites with different glucose contents

The Fig. 5 displays the XRD patterns of MoS_2 with varying carbon levels within the angle range of 5° to 70°. We can observe that the main diffraction peak of MoS_2 located at 14.1°, which corresponds to the (002) crystal plane, exhibits a significant leftward shift.

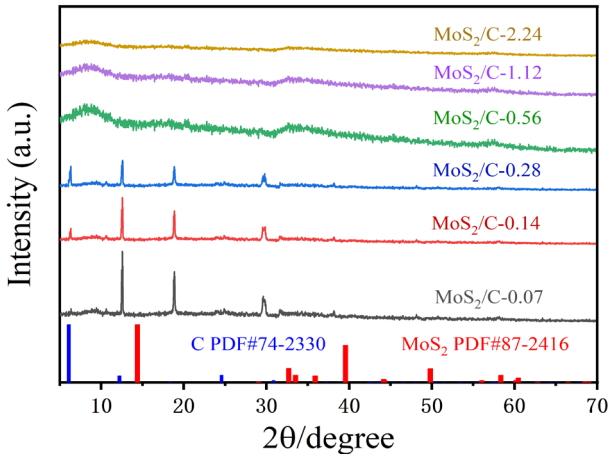

Fig. 5. XRD patterns of MoS_2/C composites with different glucose contents.

This is most likely attributed to the fact that during the complexation of MoS_2 with carbon, carbon atoms, as well as other possible heteroatoms, are doped into the MoS_2 crystals, which changes the parameters of the crystal cell and affects the position of the diffraction peaks. With the gradual increase of glucose addition, the diffraction peak at 6.1° becomes sharper and sharper, which is consistent with the characterization of the (002) crystal surface in the PDF card (PDF#74-2330), indicating a gradual increase of carbon content in the sample. When the addition of glucose reached a critical value, roughly 0.56 mmol, the XRD patterns of the samples exhibited very different characteristics. The originally sharp diffraction peaks begin to flatten out, suggesting a significant change in the internal structure of the sample. This is mainly due to the effective blocking effect on the stacking behavior of MoS_2 nanosheets as the carbon content continues to increase. This change triggers a gradual evolution within the sample, leading to the emergence of multiple phases with similar lattice structures and diffraction angles. On the XRD pattern, the diffraction peaks corresponding to these phases overlap with each other, causing the originally distinct and identifiable diffraction peaks to become blurred and difficult to distinguish.

Electron microscopy was conducted on six groups of MoS_2/C composites to examine their microstructural features, with carbon concentrations labeled a, b, c, d, e, and f from low to high. As can be seen in Fig. 6, when the glucose concentration is low, the MoS_2/C composite material is a small ball of flower ball, the ball morphology is more regular, and the independence is good, and when the glucose concentration is high, the ball morphology is destroyed, and a large number of different sizes can be seen in the figure, with many lumps of different morphology, which may be the result of too much glucose added, and glucose is hydrothermally decomposed, which then makes the carbon material attached to the MoS_2.

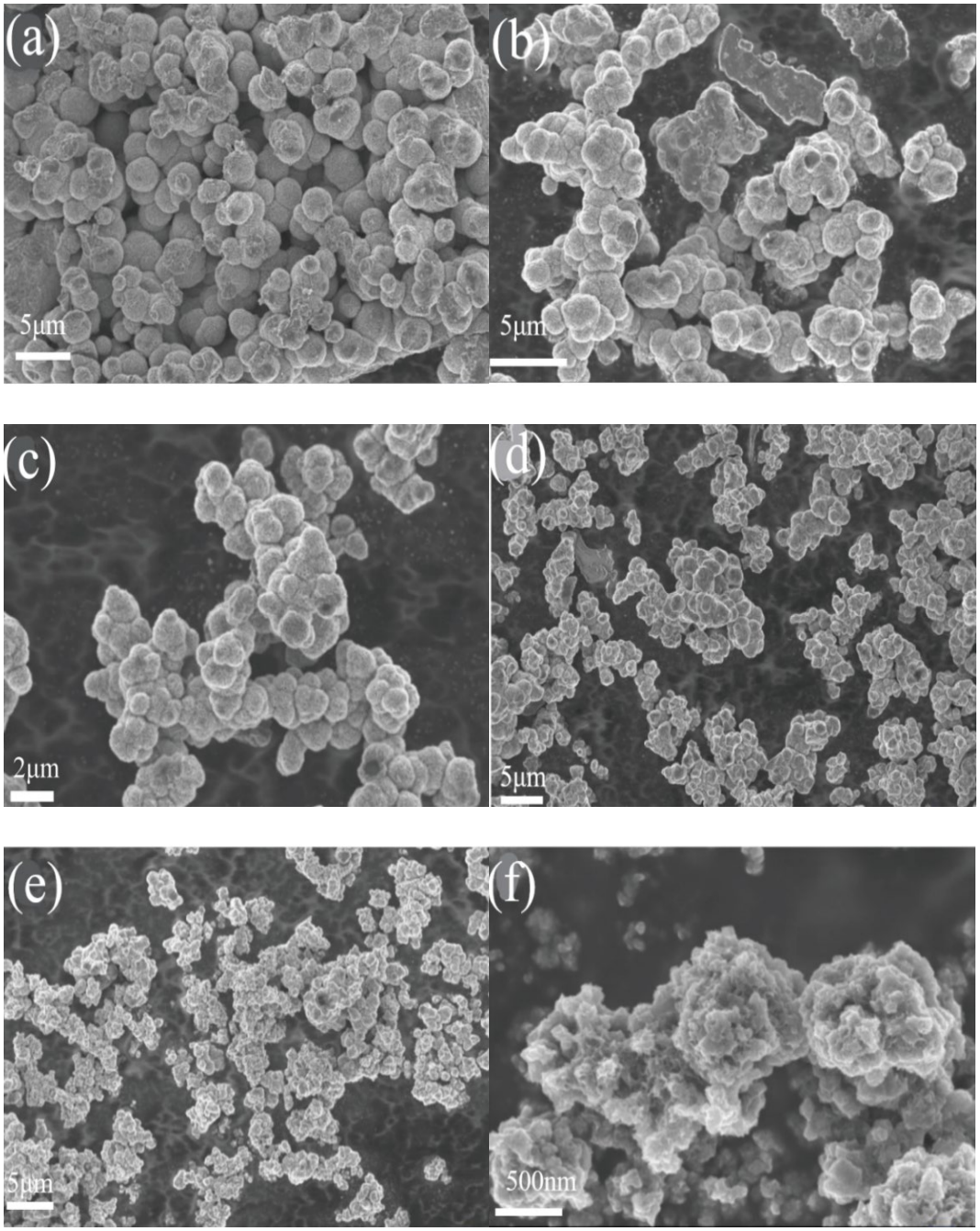

Fig. 6. SEM images of MoS_2/C composites with different glucose contents. The glucose concentrations corresponding to a, b, c, d, e, and f are 0.07 mmol, 0.14 mmol, 0.28 mmol, 0.56 mmol, 1.12 mmol, 2.24 mmol.

It may be that the amount of glucose added is too large, the hydrothermal decomposition of glucose occurs, and then the carbon material adheres to the MoS_2, which prevents the growth of molybdenum disulfide, or it may be that the viscosity of glucose itself makes it stick together, resulting in the change of morphology.

To confirm the accuracy of the XRD results and further examine the elemental composition and chemical state of the MoS_2/C composites, XPS characterization was conducted, as illustrated in Fig. 7 (d). It demonstrates the presence of C, S and Mo. The XPS instrument may have certain errors during the measurement process, such as energy scale shift, inconsistency of sensitivity, etc. The state of contamination and oxidation of the sample surface may likewise affect the XPS measurement results. The signal strength of carbon, as a widely occurring element, can be used as a reference for the surface state of the sample. With carbon correction, the known properties of elemental carbon (e.g., the binding energy of carbon is usually about 284.8 eV) can be utilized as a reference to correct for errors, thereby improving the accuracy of the measurement results [48-50]. Three peak patterns, 284.8, 285.5, and 288.6 eV, corresponding to C-C, C-O, and C=O, respectively, are observed in the C 1s high-resolution Fig 7 (a).

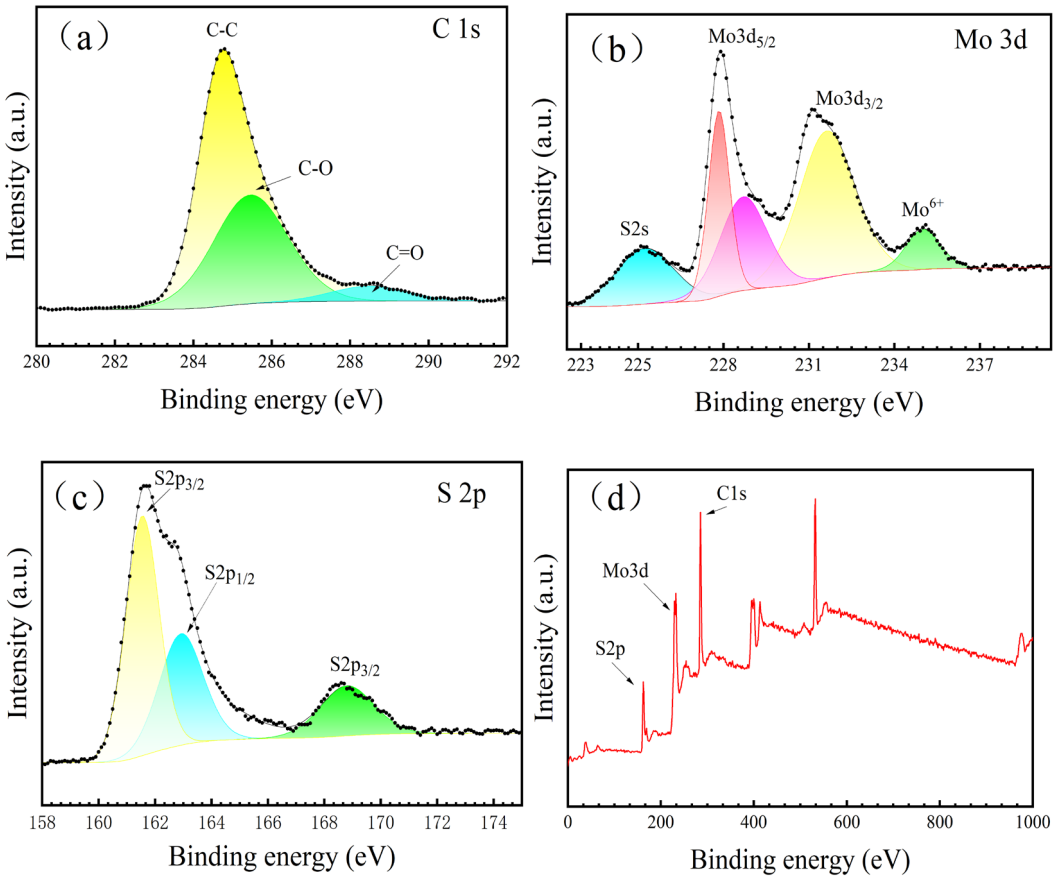

Fig. 7. (a) C 1s (b) Mo 3d (c) S 2p (d) Total XPS spectra of MoS_2/C composite materials.

In the Mo 3d high resolution Fig 7 (b), three peaks of 227.9, 231.1, and 235.1 eV can be observed, representing $Mo3d_{5/2}$, $Mo3d_{3/2}$, and $Mo^{6+}3d_{3/2}$, respectively, where the formation of the $Mo^{6+}3d_{3/2}$ electronic state mainly results from the oxidation of Mo^{4+} ions on the surface of the material upon exposure to air. This oxidation process results in the loss of electrons from the Mo^{4+} ions, which in turn transforms into the Mo^{6+} ionic state and is accompanied by a corresponding adjustment of the electronic structure, as evidenced by the formation of the $3d_{3/2}$ electronic state. There are three peak patterns of 161.8, 162.9, and 168.8 eV in the S 2p high-resolution Fig 7 (c),

representing $S2p_{3/2}$, $S2p_{1/2}$, and S-O, respectively. The formation of S-O mainly occurs because S atoms on the surface or edges of MoS_2 may react with oxygen molecules (O_2) to form S-O bonds when exposed to oxygen-containing environments. In the process of preparing or treating MoS_2, it may also create some defects or vacancies that are more likely to combine with oxygen atoms to form S-O bonds.

Cyclic voltammetry was performed on MoS_2 electrode materials with varying glucose concentrations at a scan rate of 10 mV/s, resulting in the data shown in Fig. 8 (a). It can be seen that the CV curves of MoS_2/C composites with different glucose contents also have significant differences, but their general shapes are all approximately rectangular shapes, indicating that they carry out the double electric layer reaction, which is not a pseudocapacitive reaction for the storage of electrical energy through the double electric layer energy storage mechanism [51]. And the CV curves formed by forward and reverse scanning show good symmetry, indicating good reversibility[52]. The electrode material's specific capacitance correlates with the measured CV curve area, as per Equation 1-1. When comparing the area of the CV curve at the same scanning rate, it can be concluded that with the addition of 0.28 mmol glucose, the sample exhibits a relatively large specific capacitance.

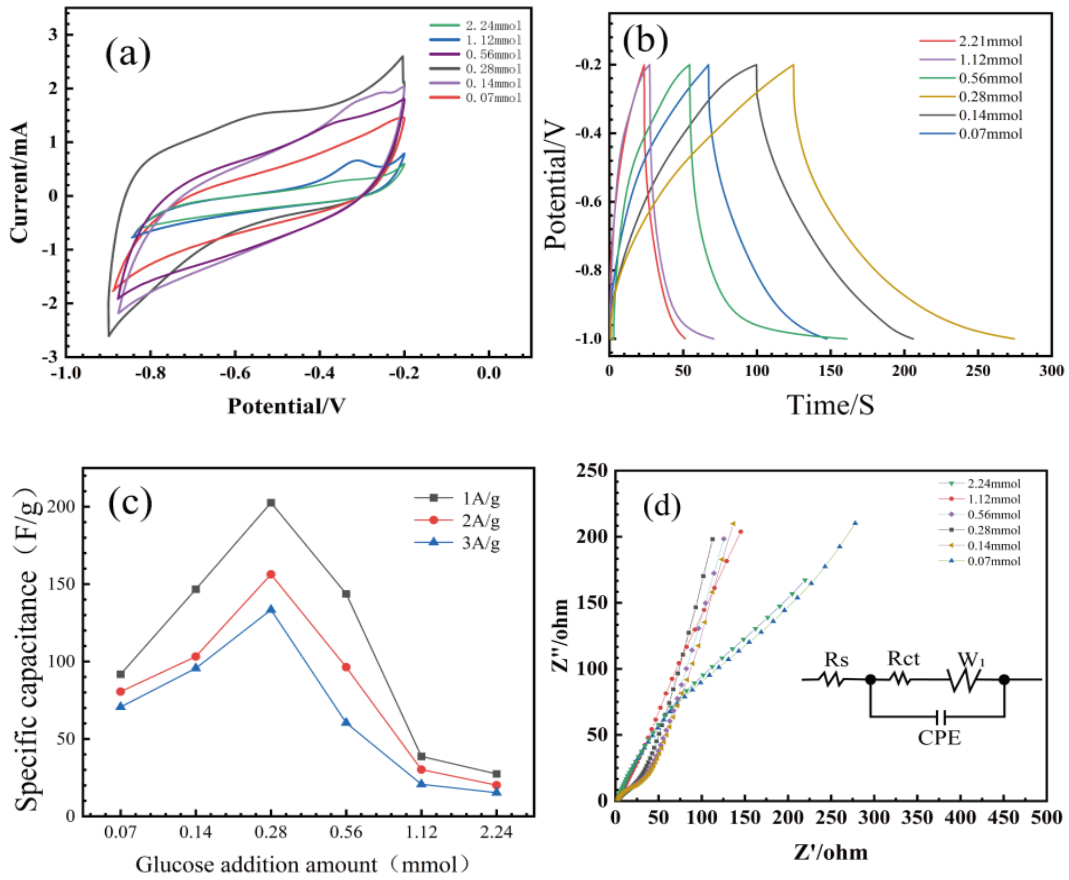

Fig. 8. (a) CV curves of MoS_2/C composites with different glucose additions; (b) GCD curves of MoS_2/C composite with different glucose additions; (c) Specific capacitance at different current densities; (d)EIS curves of MoS_2/C composite with different glucose additions.

Fig. 8 (b) displays the gcd curves of MoS_2 composite electrode materials with the same glucose addition at a current density of 1 A/g. The GCD curves of the electrode materials prepared with different glucose additions are all approximate isosceles triangles. The charging time is basically the same as the discharging time, indicating that the electrode material has a high Coulombic efficiency, showing a good stability of charging and discharging to bilayer energy storage [53-55]. Calculations based on Eqs. 1-2 show that the specific capacitance can reach 91.13 F/g, 146.68 F/g, 202.6 F/g, 143.67 F/g, 38.7. F/g, 27.24 F/g when the glucose addition is 0.07 mmol, 0.14 mmol, 0.28 mmol, 0.56 mmol, 1.12 mmol, and 2.24 mmol, respectively, 59.8 F/g, which is also consistent with the results of the CV curves. The continuous increase in glucose addition leads to a significant rise in the specific capacitance of the electrode material, reaching its peak at an addition amount of 0.28 mmol within this group. As the amount of glucose added further rises, the electrode material's specific capacitance progressively declines. Fig. 8 (c) illustrates the specific capacitance trends of the samples across varying current densities. Notably, the highest capacitance value is observed when 0.28 mmol of glucose is added, regardless of the current density.It can also be clearly seen that the specific capacitance of the MoS_2/C composite electrode materials with different glucose additions all decreased to a certain extent as the current density increased, but compared with MoS_2 alone, the specific capacitance retention has been greatly improved.

To further investigate the electrochemical performance of composite electrode materials with varying glucose content, impedance analysis of the AC curve was conducted. Fig. 8 (d) depicts the Nyquist diagram of MoS_2/C composite electrode materials at different levels of glucose addition. The experiment utilized a starting frequency of 100 kHz and a stopping frequency of 0.01Hz. The Nyquist diagram includes a high-frequency semicircle for charge transfer resistance (Rct) and a low-frequency straight line for Warburg impedance (Zw). It is evident that there is minimal variation in the semicircular radius, indicating consistent charge transfer resistance, but significant differences in the linear slope, reflecting variations in electrolyte ion diffusion within the electrode material [56-59]. At a glucose addition level of 0.28 mmol, the slope was highest, signifying the fastest diffusion rate; however, as glucose addition increased, diffusion rate gradually decreased due to potential reduction in pore volume and porosity along with carbon-induced blockage hindering electrolyte ion diffusion to the electrode.

4. Conclusions

In summary, a one-step hydrothermal method was used to prepare MoS_2/C composites, utilizing ammonium molybdate, thiourea, carbamide, and glucose as raw materials. These composites were then employed as supercapacitor electrode materials and characterized by XRD, SEM, and electrochemical tests. The following conclusions were obtained: when ethanol and deionized water were used as solvents, the solvent environment had a greater effect on the structure and morphology of the material, and when ethanol was used as a solvent, the material showed a smoother spherical structure, but its specific surface area was small, and more impurities appeared in the product, which decreased the purity of the product; When deionized water was used as the solvent, the material appeared to be in the form of a flower sphere composed of lamellar structures, with a large specific surface area and a high purity of the product.

By changing the amount of glucose to change the carbon content, we found that the glucose content has a great influence on the surface morphology of the material. When the glucose content is less, the MoS_2/C composites are small spherical spheres with more regular spherical morphology and good independence, whereas when the glucose concentration is high, the spherical morphology is destroyed, with different sizes and irregular shapes of small pieces, which have many small particles on their surfaces, making the petal-like nanosheet structure disappear. The specific capacitance and other properties showed a trend of increasing and then decreasing with increasing glucose content, where the maximum MoS_2/C specific capacitance reached 202.6 F/g at a glucose concentration of 0.28 mmol.

Acknowledgements

This work was supported by Taishan Industrial Leading Talents Program of Shandong Province(No.tscx202306082), Qilu University of Technology (Shandong Academy of Sciences)-Weihai City Industry-University-Research Collaborative Innovation Fund (2022CXY-03) and Innovation Training Program for College Students at Qilu University of Technology.

References

[1] Zhu Wenjun, Zhao Junyao, Tao Xinyong, Journal of Energy Storage, 84(2024); https://doi.org/10.1016/j.est.2024.110934

[2] Bongu Chandra Sekhar, Krishnan Mohan Raj, Soliman Abdelrahman, Arsalan Muhammad, Alsharaeh Edreese H., ACS Omega, 8(40), 36789-800 (2023); https://doi.org/10.1021/acsomega.3c03370

[3] Niaz Niaz Ahmad, Shakoor Abdul, Hussain Fayyaz, Ali Syed Mansoor, Mahmood Umar, Inoishi Atsushi, Khalil Rana Muhammad Arif, Gregory Duncan H., Journal of Materials Science: Materials in Electronics, 34(28), (2023); https://doi.org/10.1007/s10854-023-11212-0

[4] Bahar Necmiye, Ekinci Duygu, Journal of Electronic Materials, 53(3), 1476-86 (2024); https://doi.org/10.1007/s11664-023-10874-0

[5] Umar Ahmad, Ahmed Faheem, Ullah Nabi, Ansari Sajid Ali, Hussain Shahid, Ibrahim Ahmed A., Qasem Hussam, Kumar Sundararajan Ashok, Alhamami Mohsen A., Almehbad Noura, Algadi Hassan, Almas Tubia, Selim Amal F., Baskoutas Sotirios, Electrochimica Acta, 479(2024); https://doi.org/10.1016/j.electacta.2023.143743

[6] Sheng Wan, Hanbo Wang, Dongyu Pei, Ziming Wang, Zhitian Fan, Mingrui Yu, Kechang Li, Haiyan Lu, Surfaces and Interfaces, 46(2024); https://doi.org/10.1016/j.surfin.2024.104049

[7] Farma Rakhmawati, Valensia Indira, Apriyani Irma, Deraman Mohamad, Awitdrus, Taer Erman, Journal of Electronic Materials, 53(3), 1487-97 (2024); https://doi.org/10.1007/s11664-023-10880-2

[8] Phan Thi Thu Trinh, Hwang Inseong, Nguyen My Thi Ngoc, Nguyen Trong Danh, Lee Jaewoong, Lee Jun Seop, Journal of Materials Science, 59(6), 2483-96 (2024).

[9] Chanu Sagolsem Nonganbi, Jha Shubham, Devi Pukhrambam Sushma, Swain Bibhu Prasad,

Bulletin of Materials Science, 47(1), (2024); https://doi.org/10.1007/s12034-023-03099-8

[10] Li Lanlan, Shao Liangna, Sun Yuxin, Yuan Ding, Jiao Zhixuan, Sun Yi, Tian Xinquan, Fei Tiancheng, Peng Yaqi, Zhang Lei, Xu Xiaobing, Journal of Alloys and Compounds, 983(2024); https://doi.org/10.1016/j.jallcom.2024.173883

[11] Manquian Carolina, Navarrete Alberto, Vivas Leonardo, Troncoso Loreto, Singh Dinesh Pratap, Nanomaterials, 14(4), (2024); https://doi.org/10.3390/nano14040353

[12] Aswathy N. R., Divakaran Nidhin, Ajay kumar P. V., Kumar Anmol, Sudha G. S., Mohanty Smita, Palai Akshaya Kumar, Journal of Energy Storage, 84(2024); https://doi.org/10.1016/j.est.2024.110946

[13] Islam Muhammad Rakibul, Bhuiyan Mahabub Alam, Ahmed Md Hasive, Rahaman Mizanur, Heliyon, 10(4), (2024); https://doi.org/10.1016/j.heliyon.2024.e26631

[14] Zhang Ru, Wu Chengfeng, Yang Wenyan, Yao Chunhuai, Jing Yidan, Yu Ningya, Su Shengpei, Mahmud Sakil, Zhang Xiaomin, Zhu Jin, Industrial Crops and Products, 210(2024); https://doi.org/10.1016/j.indcrop.2024.118187

[15] Yu Hongquan, Tian Zhuang, Zhao Hengyan, Wu Yanbo, Chen Baojiu, Xu Sai, Zhang Yong, Zhao Hong, Ceramics International, 49(1), 1203-13 (2023); https://doi.org/10.1016/j.ceramint.2022.09.098

[16] Joshi Bhavana, Samuel Edmund, Kim Yongil, Kim Taegun, El-Newehy Mohamed, Aldalbahi Ali, Yoon Sam S., International Journal of Energy Research, 46(15), 22100-12 (2022); https://doi.org/10.1002/er.7719

[17] Yang C. H., Hsiao Y. C., Lin L. Y., ACS Appl Mater Interfaces, 13(35), 41637-48 (2021); https://doi.org/10.1021/acsami.1c10985

[18] Gao Xicheng, Bi Jianqiang, Xie Lulin, Liu Chen, Rong Jiacheng, Che Chengjiao, Leung Suwing, Journal of Power Sources, 591(2024); https://doi.org/10.1016/j.jpowsour.2023.233838

[19] Jia Feifei, Sun Kaige, Yang Bingqiao, Zhang Xian, Wang Qingmiao, Song Shaoxian, Desalination, 446，21-30 (2018); https://doi.org/10.1016/j.desal.2018.08.024

[20] Rozenfeld Shmuel, Teller Hanan, Schechter Michal, Farber Ravit, Krichevski Olga, Schechter Alex, Cahan Rivka, Bioelectrochemistry, 123201-10 (2018).

[21] Huang Huayu, Zhang Jiangyi, Cheng Meimei, Liu Kunping, Wang Xingyu, Microchimica Acta, 184(12), 4803-8 (2017); https://doi.org/10.1007/s00604-017-2531-6

[22] Wang Mingxia, Shi Yifei, Zhang Yubin, Wang Yang, Huang Huayu, Zhang Jiangyi, Song Jinxi, Electroanalysis, 29(11), 2620-7 (2017); https://doi.org/10.1002/elan.201700411

[23] Rahman Imam Abdul, Purqon Acep, Journal of Physics: Conference Series, 877(2017); https://doi.org/10.1088/1742-6596/877/1/012026

[24] Sabari Girisun T. C., Durairaj M., Vijaya S., Anandan S., Materials Science and Engineering: B, 287(2023); https://doi.org/10.1016/j.mseb.2022.116123

[25] Cao Fang, Yang Lie, Zhang Yafang, Zhao Xinya, Lu Hao, Wang Jinlong, Journal of Cleaner Production, 380(2022); https://doi.org/10.1016/j.jclepro.2022.135002

[26] R Rohith, Prasannakumar Anandhu Thejas, Mohan Ranjini R., V Manju, Varma Sreekanth J., ChemistrySelect, 7(41), (2022).

[27] Zarach Zuzanna, Szkoda Mariusz, Trzciński Konrad, Łapiński Marcin, Trykowski Grzegorz, Nowak Andrzej P., Electrochimica Acta, 435(2022);

https://doi.org/10.1016/j.electacta.2022.141389

[28] He Yang, Liu Changlin, Xie Zhengkun, Xiaokaiti Pairuzha, Chen Gang, Feng Zhongbao, Kasai Yutaka, Abudula Abuliti, Guan Guoqing, Advanced Composites and Hybrid Materials, 6(3), (2023); https://doi.org/10.1007/s42114-023-00661-0

[29] Bae Youngkuk, Seong Chae-Yong, Yoo Suyeon, Park Seung-Keun, Piao Yuanzhe, Energy Technology, 5(8), 1200-7 (2017); https://doi.org/10.1002/ente.201600502

[30] Ye Huiming, Song Liang, Zhang Fuhui, Li Juan, Su Zhiying, Zhang Yun, Analytical Sciences, 37(4), 575-80 (2020); https://doi.org/10.2116/analsci.20P297

[31] Zeng Biao, Chen Yan, Bai Jingge, Journal of Materials Science: Materials in Electronics, 30(19), 17706-14 (2019); https://doi.org/10.1007/s10854-019-02120-3

[32] Sarmah Devalina, Kumar Ashok, Electrochimica Acta, 312392-410 (2019).

[33] Wang Chuan, Huang Jinzhao, Chen Jiayue, Xi Zhongxin, Deng Xiaolong, Frontiers in Chemistry, 7(2019); https://doi.org/10.3389/fchem.2019.00131

[34] Vilian A. T. Ezhil, Dinesh Bose, Kang Sung-Min, Krishnan Uma Maheswari, Huh Yun Suk, Han Young-Kyu, Microchimica Acta, 186(3), (2019); https://doi.org/10.1007/s00604-019-3287-y

[35] Vasilescu Ioana, Eremia Sandra A. V., Kusko Mihaela, Radoi Antonio, Vasile Eugeniu, Radu Gabriel-Lucian, Biosensors and Bioelectronics, 75232-7 (2016).

[36] Alsaiari Mabkhoot, Imran Muhammad, Afzal Amir Muhammad, Iqbal Muhammad Waqas, Algethami Jari S., Harraz Farid A., Materials Today Chemistry, 35(2024); https://doi.org/10.1016/j.mtchem.2024.101909

[37] Yadav Rimjhim, Saini Ayushi, Choudhary Jyoti, Sardana Silki, Ohlan Anil, Singh Kuldeep, Singh Surinder P., Energy Storage, 5(8), (2023); https://doi.org/10.1002/est2.477

[38] Chen Ming, Deng Songlin, Qing Yan, Xu Han, Liao Yu, Li Lei, Zhang Zhen, Yan Ning, Tian Cuihua, Wu Ying, Wu Yiqiang, Carbohydrate Polymers, 294(2022); https://doi.org/10.1016/j.carbpol.2022.119754

[39] Ghanashyam Gyawali, Kim Haekyoung, Journal of Power Sources, 596(2024); https://doi.org/10.1016/j.jpowsour.2024.234088

[40] Sun Haohao, Ji Xinyang, Qiu Yunfeng, Zhang Yuanyuan, Ma Zhuo, Gao Guang-gang, Hu PingAn, Journal of Alloys and Compounds, 777514-23 (2019).

[41] Ma Wei, Li Huanran, Jiang Suyu, Han Guihong, Gao Jian, Yu Xiaomei, Lian Honglei, Tu Weifeng, Han Yi-fan, Ma Renzhi, ACS Sustainable Chemistry & Engineering, 6(11), 14441-9 (2018); https://doi.org/10.1021/acssuschemeng.8b03111

[42] Heiba Asmaa R., Abou Shahba Rabab M., Dhmees Abdelghaffar S., Taher Fatma A., El Sawy Ehab N., Journal of Energy Storage, 83(2024); https://doi.org/10.1016/j.est.2024.110762

[43] Baby Anjana, Vigneswaran J., Jose Sujin P., Davis Deljo, Pb Sreeja, Materials Today Sustainability, 26(2024); https://doi.org/10.1016/j.mtsust.2024.100727

[44] Carvalho José Tiago, Correia Afonso, Cordeiro Neusmar J. A., Coelho João, Lourenço Sidney A., Fortunato Elvira, Martins Rodrigo, Pereira Luís, npj 2D Materials and Applications, 8(1), (2024); https://doi.org/10.1038/s41699-024-00448-x

[45] Chen Guoqing, Liu Zhenlu, Yang Guangjie, Zhang Qian, Lan Tiancheng, Zhang Chunmei, Li Ping, Liu Kunming, He Shuijian, Colloids and Surfaces A: Physicochemical and Engineering Aspects, 687(2024); https://doi.org/10.1016/j.colsurfa.2024.133498

[46] Fu Xiu-Yan, Shu Ruo-Yu, Ma Chang-Jing, Jiang Hao-Bo, Yao Meng-Nan, Electrochimica Acta, 481(2024); https://doi.org/10.1016/j.electacta.2024.143987

[47] Irfan Muhammad, Sarfraz Fariha, Tariq Ammar, Waqas Umer, Ramay Shahid M., Afzal Fatima, Atiq Shahid, Diamond and Related Materials, 144(2024); https://doi.org/10.1016/j.diamond.2024.110948

[48] Greczynski G., Hultman L., Progress in Materials Science, 107(2020); https://doi.org/10.1016/j.pmatsci.2019.100591

[49] Lee Dooyong, Park Sungkyun, Current Applied Physics, 6425-33 (2024).

[50] Bagus Paul S., Freund Hans-Joachim, Surface Science, 745(2024); https://doi.org/10.1016/j.susc.2024.122471

[51] Jiang Jin, Wang Mengyao, Zhao Wenli, Cao Yu, Shi Rui, Wang Zhi, European Polymer Journal, 208(2024); https://doi.org/10.1016/j.eurpolymj.2024.112856

[52] Kumar Nitish, Ansari Mohd Rehan, Khaladkar Somnath, Maurya Oshnik, Peta Koteswara Rao, Kalekar Archana, Singha Monoj Kumar, Dash Jatis Kumar, Materials Chemistry and Physics, 316(2024); https://doi.org/10.1016/j.matchemphys.2024.129072

[53] Li Han, Yuan Xulong, Wei Zibo, Shi Jianguo, Jia Qingling, Ma Dong, Li Yong, Zhang Yongxing, Zhu Xuebin, Materials Today Chemistry, 37(2024); https://doi.org/10.1016/j.mtchem.2024.102002

[54] Mascarenhas Fiona Joyline, Rodney John D., Kim Byung Chul, Bhat Badekai Ramachandra, Journal of Alloys and Compounds, 986(2024); https://doi.org/10.1016/j.jallcom.2024.173957

[55] Nie Weidong, Liu Yuanyuan, Li Jing, Wang Meiri, Liu Kaihua, Cui Hongtao, Journal of Alloys and Compounds, 984(2024); https://doi.org/10.1016/j.jallcom.2024.174027

[56] Noor Navid, Baker Thomas, Lee Hyejin, Evans Elliot, Angizi Shayan, Henderson Jeffrey Daniel, Rakhsha Amirhossein, Higgins Drew, ACS Omega, 9(9), 10080-9 (2024); https://doi.org/10.1021/acsomega.3c04836

[57] Revathi A., Palanisamy P. N., Boopathiraja R., Sudha D., Diamond and Related Materials, 144(2024); https://doi.org/10.1016/j.diamond.2024.110953

[58] Wang He, Wang Hongjie, Hu Chengwen, Cheng Yaling, Yao Lan, Ruan Fangtao, Feng Quan, Chu Changliu, Lin Tong, Wang Hongxia, Journal of Energy Storage, 84(2024); https://doi.org/10.1016/j.est.2024.110960

[59] Zhao Chongjun, Li Mingkun, Guo Huiming, Tong Xiangzhi, Gao Wenjie, Zhao Chunhua, Journal of Energy Storage, 84(2024); https://doi.org/10.1016/j.est.2024.110950